Physics and Imaging in Radiation Oncology 6 (2018) 14–19

Contents lists available at ScienceDirect

Physics and Imaging in Radiation Oncology

journal homepage: www.elsevier.com/locate/phro

Original Research Article

Comparison of single and dual energy CT for stopping power determination in proton therapy of head and neck cancer

Vicki Trier Taasti[a,*], Ludvig Paul Muren[a,1], Kenneth Jensen[b], Jørgen Breede Baltzer Petersen[a], Jesper Thygesen[c], Anna Tietze[d,e], Cai Grau[b], David Christoffer Hansen[a]

[a] Dept. of Medical Physics, Aarhus University Hospital, Aarhus, Denmark
[b] Dept. of Oncology, Aarhus University Hospital, Aarhus, Denmark
[c] Dept. of Clinical Engineering, Aarhus University Hospital, Aarhus, Denmark
[d] Dept. of Neuroradiology, Aarhus University Hospital, Aarhus, Denmark
[e] Institute of Neuroradiology, Charité – Universitätsmedizin Berlin, Berlin, Germany

ARTICLE INFO

Keywords:
Proton therapy
Stopping power ratio
Dual-energy CT
Water-equivalent path length
Head and neck cancer

ABSTRACT

Background and purpose: Patients with head and neck (HN) cancer may benefit from proton therapy due to the potential for sparing of normal tissue. For planning of proton therapy, dual-energy CT (DECT) has been shown to provide superior stopping power ratio (SPR) determination in phantom materials and organic tissue samples, compared to single-energy CT (SECT). However, the benefit of DECT in HN cancer patients has not yet been investigated. This study therefore compared DECT- and SECT-based SPR estimation for HN cancer patients.
Materials and methods: Fourteen HN cancer patients were DECT scanned. Eight patients were scanned using a dual source DECT scanner and six were scanned with a conventional SECT scanner by acquiring two consecutive scans. SECT image sets were computed as a weighted summation of the low and high energy DECT image sets. DECT- and SECT-based SPR maps were derived. Water-equivalent path lengths (WEPLs) through the SPR maps were compared in the eight cases with dual source DECT scans. Mean SPR estimates over region-of-interests (ROIs) in the cranium, brain and eyes were analyzed for all patients.
Results: A median WEPL difference of 1.9 mm (1.5%) was found across the eight patients. Statistically significant SPR differences were seen for the ROIs in the brain and eyes, with the SPR estimates based on DECT overall lower than for SECT.
Conclusions: Clinically relevant WEPL and SPR differences were found between DECT and SECT, which could imply that the accuracy of treatment planning for proton therapy would benefit from DECT-based SPR estimation.

1. Introduction

Treatment planning of proton therapy is today typically based on stopping power ratio (SPR) estimation from single-energy CT (SECT) images. The SPR is used in treatment planning to calculate the dose distribution and the proton range [1]. SPR can be estimated from a SECT scan applying a piecewise linear fit between CT numbers and SPRs, calibrated either on literature data for human tissues [2] or on measurements for tissue substitutes with known properties [3]. Using an empirical fit, all tissues cannot be estimated correctly as some tissues can have the same CT number but different SPRs or vice versa [4]. Patient-specific tissue variations can also cause large SPR estimation errors when estimated based on SECT [5]. Dual-energy CT (DECT) has been proposed by several groups for improving the SPR accuracy compared to SECT [4–8], and DECT has been shown to be superior to SECT for organic tissue samples [9–12].

DECT has been introduced into treatment planning of proton therapy [13,14]. In this clinical workflow, virtual mono-energetic images (VMIs) are used, which are comparable to SECT images acquired at a single energy instead of the full x-ray spectrum [15]. Hudobivnik et al. have compared dose calculations based on SECT and DECT scans in the brain region [16]. They found range differences on the order of 1 mm, but concluded this result to be insignificant as their DECT-based SPR estimation had an accuracy of the same order [16].

* Corresponding author.
E-mail address: victaa@rm.dk (V.T. Taasti).
[1] Dr. Ludvig Muren, a co-author of this paper, is Editor-in-Chief of Physics & Imaging in Radiation Oncology. A member of the Editorial Board managed the editorial process for this manuscript independently from Dr. Muren and the manuscript was subject to the Journal's usual peer-review process

https://doi.org/10.1016/j.phro.2018.04.002
Received 20 December 2017; Received in revised form 9 April 2018; Accepted 11 April 2018
2405-6316/ © 2018 The Authors. Published by Elsevier B.V. on behalf of European Society of Radiotherapy & Oncology. This is an open access article under the CC BY-NC-ND license (http://creativecommons.org/licenses/BY-NC-ND/4.0/).

Treatment planning comparisons have also been performed on prostate and brain tumor patients by Wohlfahrt et al. [14]. They found that the range shifts for brain tumors was 1.1 mm (1.2% of the total range) and 4.1 mm (1.7%) for prostate-cancer patients [14].

The advantages of DECT should be investigated for all potential proton therapy indications. Treatment of patients with head and neck (HN) cancer is a particular challenge due to the many critical normal tissues close to the targeted tumor-bearing volumes. These patients may therefore benefit considerably from proton therapy due to the possibility of improved normal tissue sparing [17]. Furthermore, it has been shown that larger range margins (up to around 6% + 1 mm) were needed in the HN region [18]. Accurate SPR calculation has therefore a considerable potential for these patients. DECT- and SECT-based SPR determination for the HN region has so far only been compared in a head phantom, indicating that DECT is superior to SECT, especially in heterogeneous regions [19]. The aim of this study was to compare DECT- and SECT-based SPR estimation in a cohort of HN cancer patients, in terms of water-equivalent path lengths (WEPLs) and SPR distributions in selected anatomical regions with homogeneous density. As the superiority of DECT has already been established in theoretical, phantom and animal tissue evaluations [4–7,9–11], any SPR deviations between DECT and SECT will be considered to be in favor of DECT-based proton therapy treatment planning.

2. Material and methods

2.1. Patient cohort

This study was approved by the local ethics committee in the Central Denmark Region (ESDH 1-10-72-61-16). In total, fourteen HN cancer patients were DECT scanned after written informed consent was obtained. The first eight patients were scanned with a Dual Source CT scanner (Group A) while the last six patients were scanned using a conventional SECT scanner by acquiring two consecutive scans at different kVp-settings (Group B). All patients were treated with photon-based radiotherapy, and they were scanned approximately mid-way through their treatment course (in week three or four).

2.2. SPR calculation

For the DECT-based SPR estimation, we used the method proposed by Taasti et al. [7]; the equations used for the SPR estimation were:

$$\mathrm{SPR}^{\mathrm{est}}_{\mathrm{soft}} = (1 + x_{\mathrm{s1}})u_H - x_{\mathrm{s1}}u_L + x_{\mathrm{s2}}u_L^2 + x_{\mathrm{s3}}u_H^2 + x_{\mathrm{s4}}(u_L^3 + u_H^3) \tag{1a}$$

$$\mathrm{SPR}^{\mathrm{est}}_{\mathrm{bone}} = (1 + x_{\mathrm{b1}})u_H - x_{\mathrm{b1}}u_L + x_{\mathrm{b2}}\frac{u_L}{u_H} + x_{\mathrm{b3}}(u_L^2 - u_H^2) + x_{\mathrm{b4}}(u_L^3 + u_H^3) \tag{1b}$$

The two equations were for soft and bone tissues, respectively, with the categorization of the two tissue types based on a nearest neighbor classification [20] (three nearest neighbors; more detail is given in the Supplementary Material (SM) S1.1). The calibration of these equations is described in SM S1.2.

The x-values in Eq. (1) were fitting parameters, and the u-values were so-called reduced CT numbers, which were calculated as follows:

$$u_j = \frac{\mathscr{H}_j - B_j^{tg}}{A_j^{tg}} \tag{2}$$

Here $\mathscr{H}_j$ was the CT number for the low, $j = L$, and the high, , energy spectrum, respectively. The calibration of the A- and B-parameters is described in SM S1.3.

For the SECT-based SPR estimation the stoichiometric method proposed by Schneider et al. [2] was used. Individual conversion curves were calibrated for each scanner, but the same constraints were used, whereby only the slopes of the different line segments differed. The conversion curve used for Group A can be seen in Fig. S2.1 in SM. The scanner characterization parameters, K^{ph}, K^{coh} and K^{KN}, used for the CT number prediction [2] were obtained from virtual 120 kVp SECT scans (Section 2.4) of a calibration phantom, Gammex Cone-Beam Electron Density Phantom (Gammex Inc., Middleton, WI).

2.3. DECT and SECT comparison

We calculated water-equivalent path lengths (WEPLs) from the DECT- and SECT-based SPR maps. The WEPLs were calculated along the proton beam paths through the entire slice using the Radon transform implemented in MATLAB (The MathWorks Inc., Natick, MA), for angles in the interval from 0° to 175° in steps of 5°. The projections through the SPR maps were multiplied by the pixel size to get WEPLs in millimeter. WEPLs equal to zero (i.e. proton paths entirely outside the body outline) in the SECT-based SPR maps were removed from the WEPL comparison.

WEPL difference maps were generated by subtracting the SECT- from the DECT-based WEPL map. The WEPL differences were reported as the root-mean-square (RMS) of the difference map, as well as RMS difference relative to the RMS of the DECT-based WEPL map, and as the 2.5% and 97.5% percentiles of the WEPL difference distributions to show the variation.

To compare the SPR directly, regions-of-interest (ROIs) were placed in reasonably homogeneous tissue regions, cranium bone, brain and eyes. The cranium bone was segmented using the bone classification applied in the DECT-based SPR method (SM S1.1). Only slices in the upper part of the head were included in the analysis, from the top of the eyes and upwards. The brain was segmented by placing a circular ROI in eight consecutive slices in the homogeneous brain region above the level of the lateral ventricle, and a circular ROI was placed in each eye in 3–5 slices.

The SPR comparison between the DECT- and SECT-based methods were based on mean SPR values over the ROIs. The SPR difference was taken relative to the mean SPR in the DECT-based SPR maps:

$$\Delta\mathrm{SPR} = \frac{\langle \mathrm{SPR}_{\mathrm{DECT}} \rangle - \langle \mathrm{SPR}_{\mathrm{SECT}} \rangle}{\langle \mathrm{SPR}_{\mathrm{DECT}} \rangle} \cdot 100\% \tag{3}$$

where $\langle ... \rangle$ denoted the mean over the ROI.

To quantify the uncertainty in the calculation caused by noise in the SPR maps, the standard error of the mean (SEM) was derived based on error propagation for the standard deviation, σ:

$$\mathrm{SEM}(\Delta\mathrm{SPR}) = \frac{100\%}{\sqrt{N}} \sqrt{\left(\frac{\langle \mathrm{SPR}_{\mathrm{SECT}} \rangle}{\langle \mathrm{SPR}_{\mathrm{DECT}} \rangle^2}\right)^2 \cdot \sigma^2(\mathrm{SPR}_{\mathrm{DECT}}) + \left(\frac{1}{\langle \mathrm{SPR}_{\mathrm{DECT}} \rangle}\right)^2 \cdot \sigma^2(\mathrm{SPR}_{\mathrm{SECT}})} \tag{4}$$

As the SEM is used in the calculation of the confidence interval, CI-95% = $[\mu - 1.96 \cdot \mathrm{SEM}, \mu + 1.96 \cdot \mathrm{SEM}]$, the magnitude of SEM relative to the magnitude of the SPR difference, ΔSPR, indicates if the result is statistically significant.

2.4. CT scan protocols

SECT images were generated by linearly weighted summation of the low and high energy DECT images, to simulate a 120 kVp image. This procedure was chosen not to expose the patients to an unnecessarily increased dose by acquiring both a DECT and SECT scan. Yu et al. have showed that this procedure can provide the same image quality as regular SECT images [15].

Patients in Group A were scanned with a Siemens SOMATOM Definition Flash dual source CT scanner (Siemens Healthineers, Forchheim, Germany) with a tube potential pair of 100/Sn140 kVp (Sn: 0.4 mm extra tin filtration). The two DECT scans were acquired simultaneous using two x-ray tubes with a 95° separation. Virtual 120 kVp SECT scans were generated during the reconstruction process at the scanner. The mixing parameter was set to $M = 0.6$ (Eq. (5)) as

suggested for this scan protocol by Krauss et al. [21]. The mixing parameter was verified by comparing the CT numbers for the tissue equivalent inserts of the calibration phantom from a virtual and a real 120 kVp image set, where the virtual 120 kVp were based on the linear mix of the 100/Sn140 kVp image sets.

Group B was scanned with a Philips Brilliance Big Bore CT scanner (Philips Heathcare, Cleveland, OH) with a tube potential combination of 90 kVp and 140 kVp, which was the lowest and highest tube potential available on this CT scanner; no extra filtration was possible at this scanner. Generation of virtual 120 kVp images was done manually as it was not possible as part of the reconstruction at the scanner console. The optimal mixing parameter for the 90 kVp and 140 kVp images was determined by least squares fitting to the following equation [13]:

$$\mathscr{H}_{120\,\mathrm{kVp}} = M \cdot \mathscr{H}_{\mathrm{low}} + (1-M) \cdot \mathscr{H}_{\mathrm{high}} \quad (5)$$

where $\mathscr{H}_j$ is the CT number for low or high DECT image or the virtual 120 kVp image. The optimization was based on CT scans of calibration phantom at all three energies. The optimal mixing parameter was found to be $M = 0.28$. For two patients in this group, SECT scans at 120 kVp were also acquired, and these SECT scans were used to validate the virtual SECT scan derived from the DECT scans.

The dose was split equally between the 90 kVp and 140 kVp images. The tube current-time product (mAs) was set individually for the 90 kVp and 140 kVp scan to obtain the same dose-length-product (DLP) for both scans. The sum of the DLPs was equal to the DLP for a 120 kVp scan. The median temporal separation between the acquisitions of the 90 kVp and 140 kVp scans was 39 s.

All patients were fixated in thermoplastic masks (Qfix, Avondale, PA). The DECT imaging dose was matched to a regular SECT scan used for treatment planning based on the DLP. A median $CTDI_{vol}$ of 6.7 mGy (range: 4.9 to 10.3 mGy) was used, and tube modulation was used for all patients.

2.5. Image processing

The field-of-view (FOV) of the high energy image for the dual source scanner was too small to encompass the shoulders of the patients (Group A). To avoid truncation artifacts image slices which did not encompass the entire body outline and the fixation devices were excluded. The shoulder slices were also removed from the images acquired at the SECT scanner (Group B). The image slices containing the uppermost part of the head was also removed. The reconstructed slice thickness was 3 mm and the rapid diameter change in this region caused partial volume averaging. Image slices in the mouth region contaminated by metal artifacts due to dental fillings were excluded for twelve patients (2–13 image slices). After image slice exclusions between 49 and 81 (median = 68) slices were used for SPR calculations.

Before the SPR calculations, the images were cropped to exclude excess air around the patients. Further, the images were segmented, and for all pixels outside body outline, the SPR was set to zero to avoid SPR comparison in non-tissue equivalent fixation devices.

Visual inspection slice by slice was performed to catch any artifacts not resulting from the SPR calculation. For one patient in Group A, motion blurring was seen around the airway in the throat which was assumed to be caused by swallowing during the image acquisition. This could occur due to the 95° separation of the two x-ray tubes for the dual source scanner, leading to a short temporal separation between acquisition of projections at the same angle for the two tubes. To exclude this motion artifact, a small square covering the affected region was copied from the SECT- to the DECT-based SPR map whereby the SPR difference in this area was zero.

The image sets for Group B showed large motion artifacts which were not foreseen. To reduce this effect, the low and the high energy image sets were rigidly registered using the MATLAB function *imregister*. For the patients where image slices in the mouth region were removed, the image registration was performed on the stack of image slices above and below the removed slices separately to avoid artifacts due to the discontinuity. The registration was not perfect, and residual artifacts were seen at the body outline and around the trachea. Due to the motion artifacts, the results for the WEPL differences for the patients in Group B were not included in the analysis.

3. Results

The largest WEPL and SPR differences between DECT and SECT were found in the air-filled cavities in the ears (Fig. 1). The median of the RMS WEPL difference across all eight patients was 1.9 mm, corresponding to a WEPL difference of 1.5% relative to the DECT-based WEPL estimate (Table 1). In general, the SPR estimates based on DECT were lower than for SECT, with the 97.5% percentile for the WEPL difference distributions just above 0 mm while the median of the 2.5% percentiles was −4.6 mm.

For all patients, the mean SPR differences over the three defined ROIs were negative showing again lower SPR estimates based on DECT compared to SECT (Table 1). The SEM for the SPR differences over the ROIs times 1.96 were less than mean differences in all cases showing that all SPR differences were statistically significant. A smaller variance was seen for the SECT-based SPR estimates extracted from the ROIs.

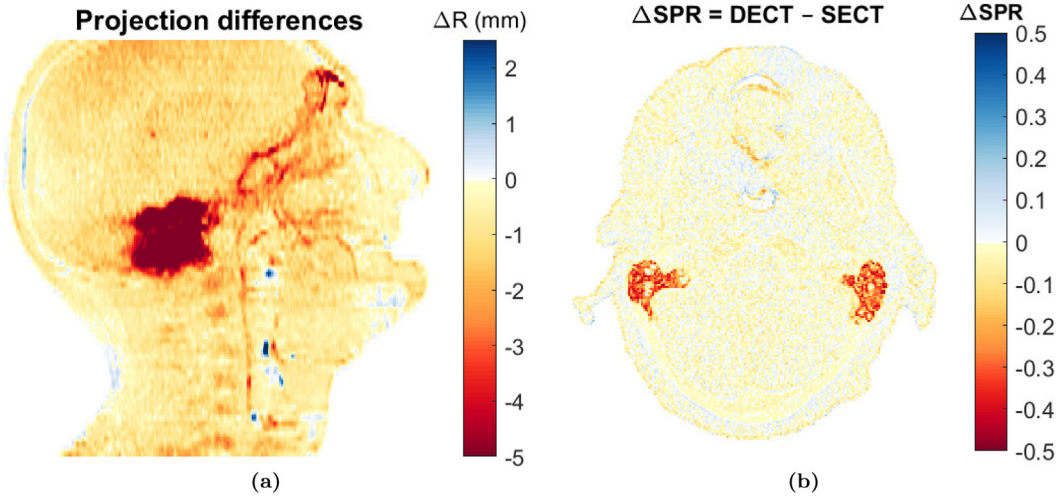

Fig. 1. Difference maps for patient No. 2. (a) WEPL difference map. (b) SPR difference map.

Table 1
WEPL and SPR differences for each individual patient. The WEPL difference is given as the RMS over all rays in absolute values (mm) (2nd column) and relative to the RMS WEPL in the DECT-based SPR map (3rd column) (%), as well as the 2.5% to 97.5% percentiles of the absolute WEPL difference (4th column). No WEPL differences are reported for Group B due to the motion artifacts. The SPR difference is given for ROIs in the cranium bone, brain and eyes (5th–7th column). The SPR difference is given relative to the DECT-based SPR (%) along with the standard error of the mean (SEM) in parenthesis (%).

	WEPL difference			SPR difference		
Patient No.	Abs. diff. (mm)	Rel. diff. (%)	Percentiles [2.5%,97.5%] (mm)	Cranium (%)	Brain (%)	Eyes (%)
			Patient subgroup A			
1	1.3	1.0	[−3.7,0.3]	0.2 (0.1)	−0.5 (0.02)	−1.5 (0.1)
2	1.8	1.4	[−4.9,0.04]	−0.2 (0.1)	−0.8 (0.02)	−1.4 (0.1)
3	2.2	1.7	[−5.8,−0.1]	−0.4 (0.1)	−1.5 (0.02)	−1.7 (0.1)
4	2.2	1.6	[−5.1,0.03]	−0.2 (0.05)	−1.2 (0.02)	−0.7 (0.2)
5	1.9	1.4	[−4.5,0.02]	−0.4 (0.05)	−1.4 (0.02)	−1.1 (0.2)
6	1.8	1.2	[−3.9,0.02]	−0.2 (0.05)	−1.4 (0.03)	−1.1 (0.1)
7	1.9	1.5	[−4.7,0.02]	−0.2 (0.1)	−1.4 (0.03)	−0.8 (0.2)
8	2.0	1.5	[−4.5,0.01]	−0.1 (0.1)	−1.4 (0.02)	−1.0 (0.2)
Median	1.9	1.5	[−4.6,0.02]	−0.2 (0.1)	−1.4 (0.02)	−1.1 (0.2)
			Patient subgroup B			
9				−1.5 (0.1)	−0.8 (0.03)	−2.0 (0.1)
10				−1.0 (0.1)	−0.9 (0.02)	−2.6 (0.1)
11				−0.4 (0.1)	−0.9 (0.03)	−2.4 (0.2)
12				−0.8 (0.1)	−0.9 (0.03)	−2.7 (0.2)
13				−1.0 (0.1)	−0.8 (0.03)	−2.6 (0.2)
14				−0.4 (0.1)	−1.2 (0.03)	−2.5 (0.2)
Median				−0.9 (0.1)	−0.9 (0.03)	−2.6 (0.2)

Fig. 2 shows examples of SPR distributions over the ROIs for one patient from each group. For brain and eyes, the SECT-based SPR distributions were very narrow, in contrast to DECT-based estimates which had larger variation; for these two organs both the SECT and DECT-based SPRs were normally distributed.

For the ROI in the cranium bone the DECT- and SECT-based SPR distributions were similar, except at the lowest SPR values, where a cut-off was seen for the SECT-based SPR distribution. Inspecting the SECT-based conversion curve (Fig. S2.A in SM), it was found that the SPR cut-off corresponded to the SPR value for the (nearly) flat piece of the curve connecting the soft and bone tissue line segments.

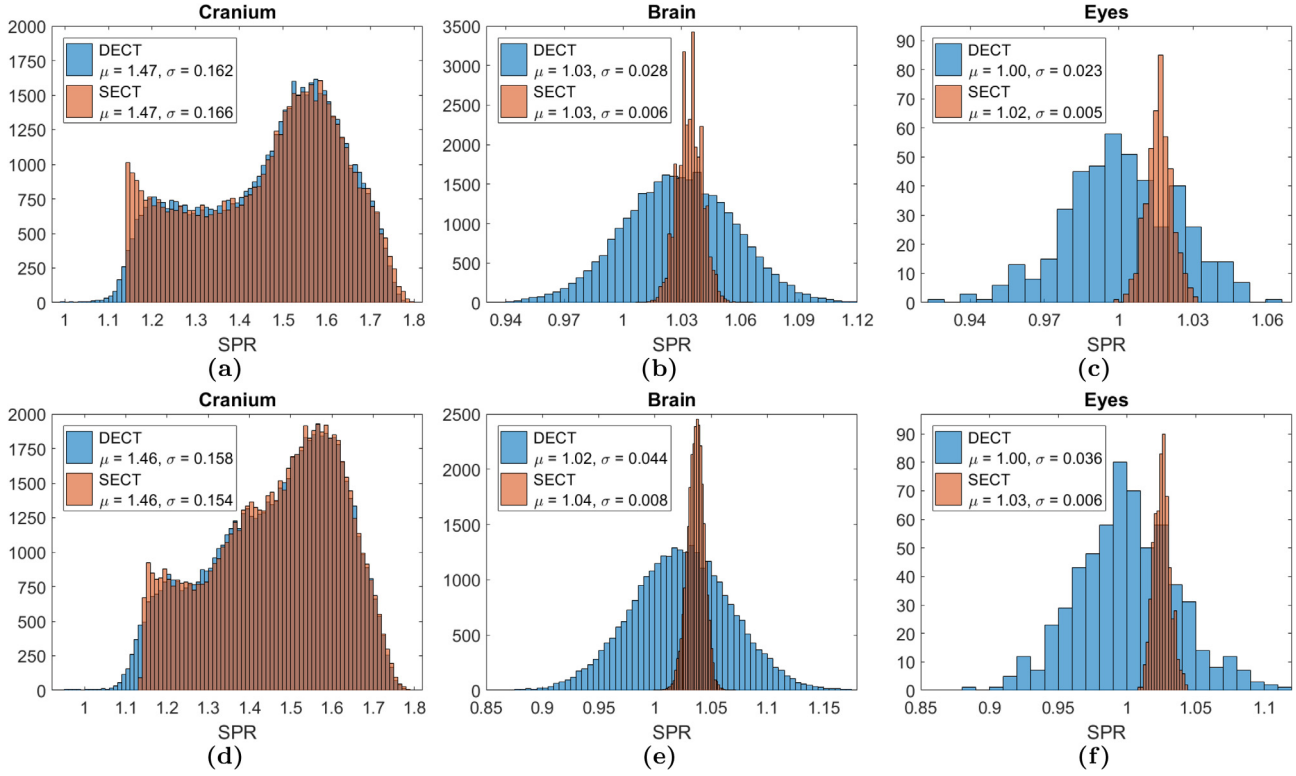

Fig. 2. SPR histograms for each ROI. The upper row is for patient No. 1, (Group A: Dual Source), and the lower row represents patient No. 14 (Group B: Consecutive Scanning). The mean (μ) and standard deviation (σ) for the distributions are given in the legends. These are most meaningful for the ROIs in the brain and in the eyes where the SPR distributions follow a normal distribution.

4. Discussion

In this study, we compared SPR and WEPL determined from DECT and SECT image sets for fourteen HN cancer patients. Statistically significant differences were seen between DECT- and SECT-based SPR estimation.

The largest WEPL and SPR differences were found in the ears (Fig. 1). Due to the very fine structures in this region, partial volume effects will occur in the transitions between bone and air. From the results reported here, it cannot be concluded which of the two SPR methods were most accurate in these structures. Mixtures of different reference human tissues were not included in the calibration of either the DECT- and SECT-based method and neither method was therefore assumed to handle partial volume effects correctly. Further investigations are warranted, and potentially special handing is needed for the SPR estimation close to transitions between air and bone.

The WEPL difference distribution was entirely situated at negative values with the median 97.5%-percentile at 0.02 mm (Table 1). The differences between the DECT- and SECT-based SPR estimation were therefore present in all structures in the HN region.

Statistically significant differences were seen between DECT- and SECT-based SPR estimation for the eyes and the brain (Fig. 2 and Table 1). This could imply a benefit of DECT. However, beam directions through the eyes would often be avoided, and for eye treatments the proton ranges are in any case very short. On the other hand, DECT could be beneficial for HN tumors near the optic pathways and base of skull. Moreover, the brain is a large organ and relevant for proton therapy. The SPR differences of 1%–1.5% (Table 1) for the brain could therefore be of clinical relevance.

It was found that the consecutive DECT scans of Group B were highly influenced by motion artifacts, which was a limitation of this study, as these artifacts excluded six of the patients from WEPL evaluations. The motion artifacts seen for Group B can be assumed to be larger than what can be expected in a standard clinical setting. Consecutive scanning DECT can be performed on dedicated scanners with an automated acquisition of both scans, which would shorten the time delay between the two acquisitions. However, motion artifacts were also seen for one patient scanned with the dual source DECT scanner despite a temporal separation of much less than a second. Consecutive scanning DECT with larger temporal separations must be used with caution.

More noise was present in the SPR maps based on DECT than on SECT, which degraded some of the fine structures in the DECT-based SPR maps. Wider SPR distributions for the brain and the eyes were also seen for DECT (Fig. 2b, c, e and f). The total dose in the DECT scan was matched to the dose used in a conventional treatment planning SECT scan. The dose in each individual DECT scan was therefore only half of the dose in a SECT scan. The SECT scans were created by weighted summation of the two DECT images, whereby the total signal was exploited, resulting in a lower noise than in either DECT image alone [15]. The wider SPR distributions for DECT therefore reflect the higher noise level. This could potentially be improved using iterative reconstruction. In this study, iterative reconstruction was not used, as CT scans were acquired from two CT scanners with different reconstruction algorithms.

Using VMIs the full imaging dose is exploited whereby VMIs will be less noisy than either of the two individual DECT images. However, using VMIs again an empirical fit between the CT numbers and the SPRs is applied and therefore SPR estimation based on VMIs does not benefit from the increased SPR accuracy obtained using a full DECT-based method.

The cut-off seen in the SPR distributions for the cranium bone (Fig. 2a and d) could imply that the line segment for the bone tissues should have been extended down to lower CT numbers, shortening the connection line between the soft and bone tissue line segments – ranging from 150 HU to 250 HU (Fig. S2.A in SM). No reference human tissues were situated in this region making it difficult to define the curve in this intermediate CT number region, as the soft and bone tissue line segments were discontinuous. It can therefore be suggested to re-evaluate the defined conversion curve based on CT scans of patients, to assess if the connection of the individual line segments is placed appropriately.

Hudobivnik et al. [16] and Wohlfahrt et al. [14] have previously performed similar studies comparing DECT- and SECT-based SPR estimation for patients, focusing on patients with brain and prostate cancer. Both studies found a range difference around 1 mm for the brain region, which was of the same order as in this study. Based on these two previous studies and our present analysis, it is apparent that DECT-based SPR estimation differs from SECT-based SPR estimation. As DECT has been shown to improve the SPR estimation [4–7,9–12,19,22,23], the benefits of DECT-based SPR estimation for proton treatment planning should be considered.

In a recent study, we found that DECT gave more accurate SPR estimates than SECT for fourteen organic tissue samples. In that study, several DECT acquisition methods including consecutive scanning and dual source, as used in this study, were evaluated, and in all cases DECT provided the best results [9]. Based on the data from this previous study, we evaluated the SPR methods used in this study. The RMSEs over all tissue samples were 0.9% and 0.8% for the DECT- and SECT-based SPR method, respectively. We therefore concluded that the applied SPR methods were appropriate for use in patients.

DECT-based SPR estimation would obviate the dependence on the definition of the conversion curve used in SECT-based estimation. Furthermore, DECT projection-based SPR methods could also be considered [24].

It should be pointed out that the noise levels in DECT must be addressed, potentially by using iterative reconstruction and/or increasing the dose level. Additionally, the DECT scanning protocol must be carefully considered, as it was shown in this study that the short temporal separation between the two consecutive scans can cause motion artifacts even in the HN region. Some of these can potentially be mitigated by applying image registration, but at best motion artifacts are avoided.

In conclusion, clinical relevant WEPL and SPR differences were found between DECT and SECT. The median WEPL difference was 1.9 mm and SPR difference were of the order of 1%. This could imply that the accuracy of proton treatment planning would improve by using DECT-based SPR estimation. Consecutive scanning should not be performed without dedicated image registration.

Conflict of interest statement

None declared.

Acknowledgements

The authors would like to thank Radiographer Torben Aagaard from Dept. of Oncology, Aarhus University Hospital for performing the CT scanning of the fourteen patients.

Appendix A. Supplementary data

Supplementary data associated with this article can be found, in the online version, at http://dx.doi.org/10.1016/j.phro.2018.04.002.

References

[1] Yang M, Zhu XR, Park PC, Titt U, Mohan R, Virshup G, et al. Comprehensive analysis of proton range uncertainties related to patient stopping-power-ratio estimation using the stoichiometric calibration. Phys Med Biol 2012;57:4095–115.
[2] Schneider U, Pedroni E, Lomax A. The calibration of CT Hounsfield units for radiotherapy treatment planning. Phys Med Biol 1996;41:111–24.
[3] Jäkel O, Jacob C, Schardt D, Karger CP, Hartmann GH. Relation between carbon ion

ranges and x-ray CT numbers. Med Phys 2001;28:701–3.
[4] Hünemohr N, Krauss B, Tremmel C, Ackermann B, Jäkel O, Greilich S. Experimental verification of ion stopping power prediction from dual energy CT data in tissue surrogates. Phys Med Biol 2014;59:83–96.
[5] Yang M, Virshup G, Clayton J, Zhu XR, Mohan R, Dong L. Theoretical variance analysis of single- and dual-energy computed tomography methods for calculating proton stopping power ratios of biological tissues. Phys Med Biol 2010;55:1343–62.
[6] Hansen DC, Seco J, Srensen TS, Petersen JBB, Wildberger JE, Verhaegen F, et al. A simulation study on proton computed tomography (CT) stopping power accuracy using dual energy CT scans as benchmark. Acta Oncol 2015;54:1638–42.
[7] Taasti VT, Petersen JBB, Muren LP, Thygesen J. Hansen DC.A robust empirical parametrization of proton stopping power using dual energy CT. Med Phys 2016;43:5547–60.
[8] Saito M, Sagara S. Simplified derivation of stopping power ratio in the human body from dual-energy CT data. Med Phys 2017;44:1465–4187.
[9] Taasti VT, Michalak GJ, Hansen DC, Deisher A, Kruse JJ, Krauss B, et al. Validation of proton stopping power ratio estimation based on dual energy CT using fresh tissue samples. Phys Med Biol 2018;63:015012.
[10] Bär E, Lalonde A, Zhang R, Jee KW, Yang K, Sharp G, et al. Experimental validation of two dual-energy CT methods for proton therapy using heterogeneous tissue samples. Med Phys 2018;45:48–59.
[11] Möhler C, Russ T, Wohlfahrt P, Elter A, Runz A, Richter C, et al. Experimental verification of stopping-power prediction from single- and dual-energy computed tomography in biological tissues. Phys Med Biol 2018;63:025001.
[12] Xie Y, Ainsley C, Yin L, Zou W, McDonough J, Solberg TD, et al. Ex vivo validation of a stoichiometric dual energy CT proton stopping power ratio calibration. Phys Med Biol 2018;63:055016.
[13] Wohlfahrt P, Möhler C, Hietschold V, Menkel S, Greilich S, Krause M, et al. Clinical implementation of dual-energy CT for proton treatment planning on pseudo-monoenergetic CT scans. Int J Radiat Oncol Biol Phys 2017;97:427–34.
[14] Wohlfahrt P, Möhler C, Stützer K, Greilich S, Richter C. Dual-energy CT based proton range prediction in head and pelvic tumor patients. Radiother Oncol 2017;125:526–33.
[15] Yu L, Primak AN, Liu X, McCollough CH. Image quality optimization and evaluation of linearly mixed images in dual-source, dual-energy CT. Med Phys 2009;36:1019–24.
[16] Hudobivnik N, Schwarz F, Johnson T, Agolli L, Dedes G, Tessonnier T, et al. Comparison of proton therapy treatment planning for head tumors with a pencil beam algorithm on dual and single energy CT images. Med Phys 2016;43:495–504.
[17] van de Water TA, Bijl HP, Schilstra C, Pijls-Johannesma M, Langendijk JA. The potential benefit of radiotherapy with protons in head and neck cancer with respect to normal tissue sparing: a systematic review of literature. Oncologist 2011;16:366–77.
[18] Schuemann J, Dowdell S, Grassberger C, Min CH, Paganetti H. Site-specific range uncertainties caused by dose calculation algorithms for proton therapy. Phys Med Biol 2014;59:4007–31.
[19] Wohlfahrt P, Möhler C, Richter C, Greilich S. Evaluation of stopping-power prediction by dual-and single-energy computed tomography in an anthropomorphic ground-truth phantom. Int J Radiat Oncol Biol Phys 2018;100:244–53.
[20] Cover T, Hart P. Nearest neighbor pattern classification. IEEE Trans Inf Theory 1967;13:21–7.
[21] Krauss B, Grant KL, Schmidt BT, Flohr TG. The importance of spectral separation: an assessment of dual-energy spectral separation for quantitative ability and dose efficiency. Invest Radiol 2015;50:114–8.
[22] Hünemohr N, Krauss B, Dinkel J, Gillmann C, Ackermann B, Jäkel O, et al. Ion range estimation by using dual energy computed tomography. Z Med Phys 2013;23:300–13.
[23] Michalak G, Taasti V, Krauss B, Deisher A, Halaweish A. McCollough C.A comparison of relative proton stopping power measurements across patient size using dual- and single-energy CT. Acta Oncol 2017;56. 4179–1471.
[24] Vilches-Freixas G, Taasti VT, Muren LP, Petersen JBB, Létang JM, Hansen DC, Rit S. Comparison of projection-and image-based methods for proton stopping power estimation using dual energy CT. Phys Imag Radiat Oncol 2017;3:28–36.